

**OPEN ACCESS**

## Overdischarge and Aging Analytics of Li-Ion Cells

To cite this article: Daniel Juarez-Robles *et al* 2020 *J. Electrochem. Soc.* **167** 090558

View the [article online](#) for updates and enhancements.



## Overdischarge and Aging Analytics of Li-Ion Cells

Daniel Juarez-Robles,<sup>1,\*</sup> Anjul Arun Vyas,<sup>1</sup> Conner Fear,<sup>1,\*\*</sup> Judith A. Jeevarajan,<sup>2,z</sup> and Partha P. Mukherjee<sup>1,\*</sup>

<sup>1</sup>School of Mechanical Engineering, Purdue University, West Lafayette, Indiana 47907, United States of America  
<sup>2</sup>Electrochemical Safety, Underwriters Laboratories Inc., Northbrook, Illinois 60062, United States of America

Overdischarge is a potential problem in large battery packs since cells in a series string are discharged under the same load, despite having different capacities. Although a single overdischarge does not necessarily cause a safety hazard, it forces electrodes outside their safe potential range and adversely affects the integrity of cell components. This work aims to fill the knowledge gap about the combined effect of aging-induced and overdischarge-induced degradation mechanisms. Graphite/LCO pouch cells are cycled at a moderate rate using four lower cutoff voltages: 2.7 V, 1.5 V, 0.0 V, and  $-0.5$  V. The cells aged above the onset of reverse potential have an extended cycle life with aging-induced solid electrolyte interphase (SEI) growth and electrolyte decomposition as the main degradation mechanisms. In contrast, the cells aged under reversal condition ( $E_{\text{lower}} \leq 0.0$  V) exhibit fast degradation, dictated by the interplay among lithium plating, cathode particle cracking, and dissolution of Cu current collector. The analysis is complemented with a comparative study of various state of health (SoH) indicators, including an internal resistance based dimensionless SoH descriptor. The results prove that overdischarge-induced abuse although benign, may turn into a malignant condition when alternated with continuous charging.

© 2020 The Author(s). Published on behalf of The Electrochemical Society by IOP Publishing Limited. This is an open access article distributed under the terms of the Creative Commons Attribution Non-Commercial No Derivatives 4.0 License (CC BY-NC-ND, <http://creativecommons.org/licenses/by-nc-nd/4.0/>), which permits non-commercial reuse, distribution, and reproduction in any medium, provided the original work is not changed in any way and is properly cited. For permission for commercial reuse, please email: [permissions@iopublishing.org](mailto:permissions@iopublishing.org). [DOI: [10.1149/1945-7111/aba00a](https://doi.org/10.1149/1945-7111/aba00a)]



Manuscript submitted March 7, 2020; revised manuscript received May 30, 2020. Published July 6, 2020. *This paper is part of the JES Focus Issue on Battery Safety, Reliability and Mitigation.*

**Safety.**—Lithium-ion batteries (LIBs) have turned into a keystone, as a power source, in the development of portable systems mainly due to their specific power and specific energy.<sup>1</sup> Their widespread usage on daily life applications along with their potential to catastrophically fail turns the safety aspects into a priority.<sup>2</sup> Some of the highly publicized events of LIB failures have drawn attention to the potential health risks that can occur. For instance, the failure on the Samsung Galaxy Note 7 batteries, due to manufacturing and design issues, led to overheating and fire.<sup>3</sup> Another incident involved the Boeing 787 Dreamliner when a flight landed in Boston and smoke was discovered in the cabin from the auxiliary power unit going into thermal runaway.<sup>4</sup> Both of these incidents involved the batteries having an unintended internal short circuit (ISC), resulting in catastrophic failure and threatening human safety.<sup>5</sup> Internal short circuit can be induced via mechanical,<sup>6</sup> thermal,<sup>7</sup> and electrochemical<sup>8</sup> abuse, typically for research purposes. However, unintended internal short circuit can occur due to several reasons and can include mishandling from the user or if the cell is inadvertently driven above (overcharge) or below (overdischarge) the safe voltage window. To prevent an internal short due to overcharging and overdischarging, the battery management system (BMS) maintains the cell within its recommended voltage window and can monitor the cells in order to detect faulty cells within a battery before they become problematic.<sup>9</sup> The BMS can also ensure that the cells are charged and discharged appropriately considering every cell within a battery will have different charge and discharge capacities.<sup>10</sup> Although it is well known that the BMS design should allow for the monitoring of individual cell/cell bank voltages, not all battery designs take that into account. An electrical load imbalance not only affects the electrochemical performance of the single cells but also its thermal response. Jeevarajan et al. showed that a single unbalanced cell in a series string can result in high temperatures throughout the string and a possible catastrophic event.<sup>11,12</sup> For that reason, it's important not only to have good control of the LIBs but also to develop a good understanding of overdischarge-induced failure and its safety implications.

**Overdischarge.**—Overdischarge is a phenomenon that occurs when a cell is discharged beyond the lower safe voltage limit determined by the electrode chemistry coupling.<sup>13</sup> Overdischarge is a potential problem in large battery packs since cells are discharged at the same rate, despite having different capacities. Consider three lithium-ion cells: two fully charged and one at 50% state of charge (SOC). If these are connected in series and then connected to an electrical load, the partially discharged cell will fully discharge before the other two and will be forced into voltage reversal by the other cells if the load is left on. Although this does not necessarily cause a safety hazard, it forces electrodes outside their normal potential range and adversely affects the cycle life.<sup>14</sup> Lai et al. showed that even a single overdischarge, if extreme enough, can permanently damage the LIB through ISC.<sup>15</sup> Jeevarajan et al. showed that overdischarging a cell within a battery pack arrangement, either series or parallel, can propagate the degradation in the surrounding cells as a result of compensating for the overdischarged cell.<sup>11</sup>

Overdischarge-induced degradation mechanisms on fresh cells have been previously studied. Maleki et al. showed that overdischarge is the factor that leads to swelling in Li-ion pouch cells due to the decomposition of the solid electrolyte interface (SEI) layer and the gases emitted from it.<sup>16</sup> Fear et al. showed that extreme overdischarge results in the dissolution of the copper (Cu) current collector from anode and deposition on the cathode, separator, and the anode surface.<sup>17</sup> They found that Cu dissolution was C-rate dependent and it takes place when the full cell voltage becomes negative and the anode potential is greater than 3.54 V vs Li/Li<sup>+</sup>.

**Cycling.**—LIBs undergo degradation even under normal cycling operation as shown by He et al. on their study of cycling of A123 18650 cylindrical cells that reduced their capacity by 20% after 1750 cycles.<sup>18</sup> The major degradation mechanisms are loss of lithium inventory and active material and degradation of the ionic and electronic elements.<sup>19</sup> Side reactions occurring between graphite and electrolyte lead to the formation of the SEI film at the surface of electrodes.<sup>20</sup> SEI prevents further corrosion of graphite and electrolyte reduction, but its continuous growth over time may affect the pore size and structure, wettability of electrolyte, contact resistance of the negative and positive electrodes, as well as the electrode porosity. Lithium plating is another side reaction consisting of the deposition of

\*Electrochemical Society Member.

\*\*Electrochemical Society Student Member.

<sup>z</sup>E-mail: [Judy.Jeevarajan@ul.org](mailto:Judy.Jeevarajan@ul.org); [pmukherjee@purdue.edu](mailto:pmukherjee@purdue.edu)

Li metal at the surface of the anode. With continuous cycling, due to the decreasing porosity of the graphite electrode and the reduced kinetics due to the increase in SEI thickness, the anode overpotential increases and the current distribution during charging becomes nonuniform.<sup>21</sup> This leads to accumulation of Li metal on the particle surface and thus leads to anode potential below 0.0 V vs Li/Li<sup>+</sup>.<sup>22</sup> Lithium plating increases at lower temperature<sup>23</sup> because of slower diffusion and increases with an increase in charging rate<sup>24</sup> as higher currents lead to an increase in the reaction rate of Li-ions at the graphite particle surface and less uniform current distribution. Lithium plating also leads to several safety issues like internal short circuit and thermal runaway. Under extreme conditions, the changes in electrode morphology due to intercalation and de-intercalation beyond their reversible limit induce mechanical stresses resulting in structural damage and cracking.

**Current work.**—Although there are extensive studies on aging-induced and overdischarge-induced degradation, there is still a knowledge gap about the effect of cycling LIBs repeatedly under an overdischarge condition. The objective of this work is to understand the degradation mechanisms of Li-ion pouch cells when cycling at different overdischarge levels. The study aims to provide insights about the possible interaction between the dissolution of Cu from the current collector and the Li plated on graphite. The interaction between cycling and overdischarge is characterized by the electrochemical performance of the full cell and morphological changes of the electrodes/separator.

### Experimental

Commercial Li-ion pouch cells obtained from a reputable vendor, with a lithium cobalt oxide (LCO) cathode and graphite (C) anode having 5.0 Ah rated capacity are used in this study. The cell has 23 double side layers of graphite, 22 double layers of LCO and two single side coated layer at the extremes. The separator is composed of polypropylene/alumina (PP/Al<sub>2</sub>O<sub>3</sub>). The electrochemical tests are carried out at ambient temperature using a battery tester (Arbin, BT-2000). The sampling rate for all tests is 1 Hz.

**Cases of study.**—As described earlier, pushing the cell to a high depth of discharge can induce dissolution of the anode copper substrate. The onset potential for copper dissolution depends upon

the electrodes active material coupling, cell configuration, and discharging rate. An upper voltage bound for this onset can be obtained by discharging the cell at a low C-rate and it ranges from  $-0.5$  to  $-1.4$  V.<sup>17</sup> In order to confirm the Cu oxidation potential for this particular coupling of electrode materials, a third electrode is incorporated in the cell. A small reference electrode (RE) made of copper wire with lithium titanate (LTO, Li<sub>4</sub>Ti<sub>5</sub>O<sub>12</sub>) active material on its flattened tip is prepared by following the method proposed by Minter et al.<sup>25</sup> The procedure ensures having a stable reference electrode potential (1.564 vs Li/Li<sup>+</sup>) throughout the different stages of overdischarge indicated in Fig. 1a. Three-electrode cell preparation and the RE insertion is conducted in an argon-filled glovebox (MBraun, H<sub>2</sub>O < 0.5 ppm, O<sub>2</sub> < 0.5 ppm). Once the reference electrode is cycled and charged up to 50% SOC, it is inserted in the pouch cell, with the copper wire extending out of the cell, and sealed with epoxy to avoid electrolyte evaporation. The cell is fully charged to 4.2 V prior to extremely overdischarging it at a C/10-rate. The cell voltage and the electrode potentials are simultaneously monitored, and the results are shown in Fig. 1a. Normal cycling occurs when the cell is operated within the manufacturer recommended voltage window, i.e.,  $E = [4.2, 2.7]$  V. This range represents the optimal electrochemical conditions where the cell will give the longest lifetime while operating safely. Slight overdischarge takes place when the cell is discharged beyond the lower recommended cutoff without reaching the reverse potential point, i.e.,  $E = [2.7, 0.0]$  V. The reverse potential point represents the condition where anode potential becomes larger than the cathode potential, as shown in Fig. 1b. The onset of reverse potential is used to distinguish between the slight and the deep overdischarge conditions.

**Cycling protocol.**—The cycling test is designed in a way that allows studying the cumulative effect of cycling at different overdischarge levels. Four lower cutoff voltages are judiciously selected according to the prior analysis:  $E_{\text{lower}} = 2.7, 1.5, 0.0$  and  $-0.5$  V. Aging dominated case,  $E = [2.7, 4.2]$  V, corresponds to cycling under the manufacturer recommended voltage window, where mostly Li<sup>+</sup> lithiation/delithiation processes and gradual SEI thickening should take place. The second case consists of a slight overdischarge condition,  $E = [1.5, 4.2]$  V, under which delithiation is expected to come along with SEI decomposition. The reverse potential onset,  $E = [0.0, 4.2]$  V, is selected as the third case of study. Under this condition, lithium inventory from graphite is

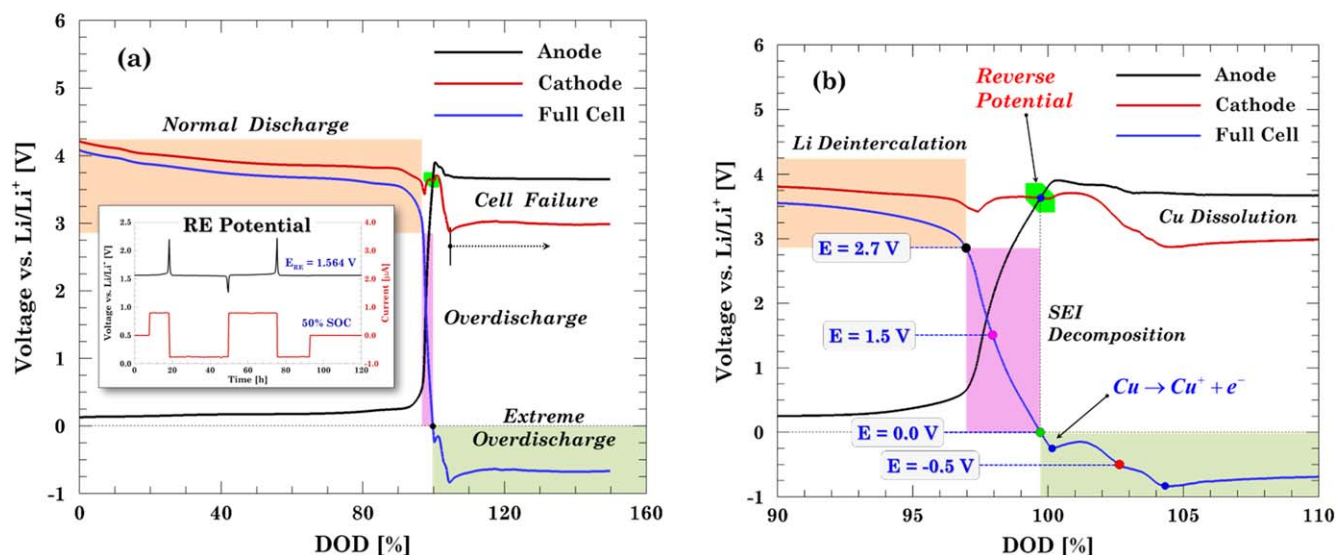


**Figure 1.** Selection of the lower cutoff voltage for the aging test under overdischarge conditions. (a) Full cell voltage and cathode and anode potentials measured during overdischarge to 150% DOD in three-electrode pouch cell, (b) degradation phenomena associated with each overdischarge stage. At the extreme overdischarge condition, the dissolution of copper and its deposition on the cathode surface shuts down the cell. Based upon these conditions, four lower cutoff voltages are selected: 2.7 V (normal discharge), 1.5 V (slight overdischarge), 0.0 V (reverse potential onset) and  $-0.5$  V (deep overdischarge).

almost depleted and SEI layer damage becomes severe. The fourth case of the study consists of a deep overdischarge condition, i.e., a discharge process far beyond from the reverse potential condition,  $E = [-0.5, 4.2]$  V. The selection of this condition is important since cyclability needs to be ensured. Previous studies have shown there is a DoD (depth of discharge) threshold after which the cell cannot be cycled any longer.<sup>17,26</sup> For this cell, the threshold voltage corresponds to the global minimum voltage from Fig. 1b,  $E = -0.832$  V (5.218 Ah  $\approx$  104% DoD). Thus, at  $-0.5$  V the cell already crossed the reverse potential condition without crossing the cell shutdown threshold. Cycling along with the overdischarge condition consists of cycling the cell at a C/10-rate under the baseline voltage window followed by 1C-rate cycles at each of the four cases described above. The initial low C-rate charging at the beginning is included to ensure a fully charged condition on the first cycle. Aging under overdischarge test is stopped when the cell exhibits a 20% capacity fade (CF) with respect to the nominal capacity (5 Ah) or in case of failure to charge.

The cell internal resistance (IR) is measured at the end of the charge,  $R_{Int,C}$ , and discharge,  $R_{Int,D}$ , using the in-built IR function from the battery system. The IR function applies 10 current pulses with a 1C-current amplitude (5 A) for a period of 100 ms. After each charge and discharge, the cell is allowed to reach thermal and electrochemical equilibrium by resting it for 25 min prior to applying the pulse-train. On every cycle, both IR values are collected and used to define the following non-dimensional parameter.

$$\Phi_R = \frac{R_{Int,C} - R_{Int,D}}{R_{Int,D}} \quad [1]$$

$\Phi_R$  was previously defined by Juarez et al. as a state of health (SoH) indicator.<sup>27</sup> The internal resistance takes its maximum values when the cell is fully charged and fully discharged. In between the two SOC extremes, the internal resistance decreases and has a bathtub like curve. As the cell degrades, the IR at the two extreme conditions will increase and  $\Phi_R$  will account for those changes.

The cell and environmental temperature are recorded with a T-type thermocouple (Omega) attached to the pouch cell surface. Heat generation is estimated from the thermal response of the cell using the inverse heat transfer method proposed by Mistry et al.<sup>28</sup> The details of the calculation and the method are similar to those described by Juarez et al. on their study on aging under different overcharge extremes.<sup>27</sup>

**Destructive physical analysis.**—At the end of the cycle life, the cells are subjected to a destructive physical analysis (DPA) in the argon-filled glovebox to further understand the failure mechanisms. The inert environment helps to preserve the evidence of degradation induced on each of the cell components for further analysis. A description of the step-by-step procedure to extract the electrodes and the separator can be found in the Appendix. All the cells are open in a fully discharged condition to reduce the ISC hazards. First, photographic evidence of the individual electrodes is taken. Then, representative samples from the electrodes and the separator are collected and analyzed via Scanning Electron Microscopy (SEM) (Hitachi S4800) and Energy Dispersive X-ray Spectroscopy (EDS) techniques. A 30 kV acceleration voltage and 10  $\mu$ A current are used to get the SEM images of the electrodes. A 10 kV acceleration voltage and 5  $\mu$ A and low vacuum conditions are used to get the SEM images of the separators.

## Results and Discussion

**Cycling performance.**—The protocol used to age the cells under an overdischarge condition is exemplified in Fig. 2a with the cycling profile corresponding to the cell cycled in the voltage range of [0.0, 4.2] V. The cycling protocol shows that extending the lower cutoff voltage from 2.7 to 0.0 V takes a short time, i.e., very little

additional capacity is gained. The plot also shows the uneven temperature rise between the charge and discharge process. Under normal cycling conditions, the temperature at the end of the discharge is greater than the one at the end of the charging process mainly due to the different intercalation rates of lithium in graphite and LCO.<sup>29</sup> In this case, the difference between maximum temperatures during discharge and charge is roughly 20 °C.

The effect of changing the lower cutoff on the cycle life is reflected on the capacity fade plot, Fig. 2b. The initial discharge capacity for each of the four cells shows a negligible increment, from 5.00 Ah to 5.33 Ah, when the lower cutoff voltage is extended from 2.7 to  $-0.5$  V. The number of times the cell can be cycled is also significantly reduced when the lower voltage is decreased. Figures 2c–2f shows the charge/discharge capacity (Q) and the coulombic efficiency ( $\eta$ ) for the cycle life for the four cycling conditions studied. On each plot, the apparent cycle where the cell starts degrading at a faster rate is indicated, based on the faster capacity fade and the maximum coulombic efficiency. The cell that was cycled under the recommended voltage window lost 20% capacity of its nominal capacity after 287 cycles, Fig. 2c. After 165 cycles, the coulombic efficiency exhibits an unsteady trend due to the degradation taking place within the cell. Similarly, for the 1.5 V case, the total number of cycles reduced to 220, Fig. 2d, and the unsteady coulombic efficiency occurs at the 145th cycle. In both cases, the main degradation mechanism is the SEI thickening. Previous studies have attributed the instability of the coulombic efficiency to the onset of lithium plating, induced by electrolyte transport restrictions related to pore clogging by the SEI.<sup>30</sup> A significant reduction in the total number of cycles occurs once the cell is driven to a reversal condition. The cell cycled at 0.0 V requires only 28 cycles to achieve the 20% CF, Fig. 2e, and the cell starts degrading faster just after 8 cycles. The cycle life gets reduced even more to 14 cycles for the deep overdischarge case at  $-0.5$  V, Fig. 2f, in which the cell degrades faster after 6 cycles. The test was stopped after the cell failed due to internal shorting. Even though lithium plating and copper dissolution simultaneously occur within the cell, the eventual cause for the cell failure is the cell swelling which finally leads to direct contact between the electrodes.

SoH estimation has a significant relevance on the safety aspects for primary use applications of LIBs and its capability to be recycled and used in a secondary application.<sup>31</sup> Unlike previous works, the present analysis focuses on analytical determination of the moment where degradation aggravates and SoH decays. An initial attempt is a differential analysis of the cycle life parameters from Figs. 2c–2f. First, discharge capacity and coulombic efficiency are fitted using third- and sixth-order polynomials, respectively, before the derivative of fitting curves is calculated. The inflection point ( $d^2Q/dN^2 = 0$ ) from the differential capacity curves, Figs. 3a–3b, indicates the point where the capacity fade rate increases. In a similar fashion, the maximum point from the differential coulombic efficiency ( $d\eta/dN = 0$ ) can be interpreted as a SoH indicator. Before this point, the low coulombic efficiency is due to a reduction of lithium inventory caused by the SEI formation.<sup>32</sup> Once the cell crosses the maximum point,  $\eta$  decreases again due to the accumulated degradation and possible occurrence of lithium plating. The flat parabolic trend of the coulombic efficiency produces the multiple zeros found in the  $d\eta/dN$  curves, Figs. 3c–3d. From all the possible zeros, the closest one to the cycle indicated in Fig. 2 is the one selected as the onset for faster degradation.

Even though IR has been previously used to investigate the effect of resistance on degradation and capacity fade,<sup>33</sup> its SOC dependence can influence the derived conclusions. IR maximizes when the cell is fully charged and fully discharged and it decreases in between.<sup>34</sup> Under normal cycling conditions, values of  $R_{Int,C}$  and  $R_{Int,D}$  are almost equal, as shown in Fig. 4a, throughout the whole cycling life. As the lower cutoff voltage is extended, Figs. 4b–4d, the charge IR remains quasi-constant and it only increases at the end of

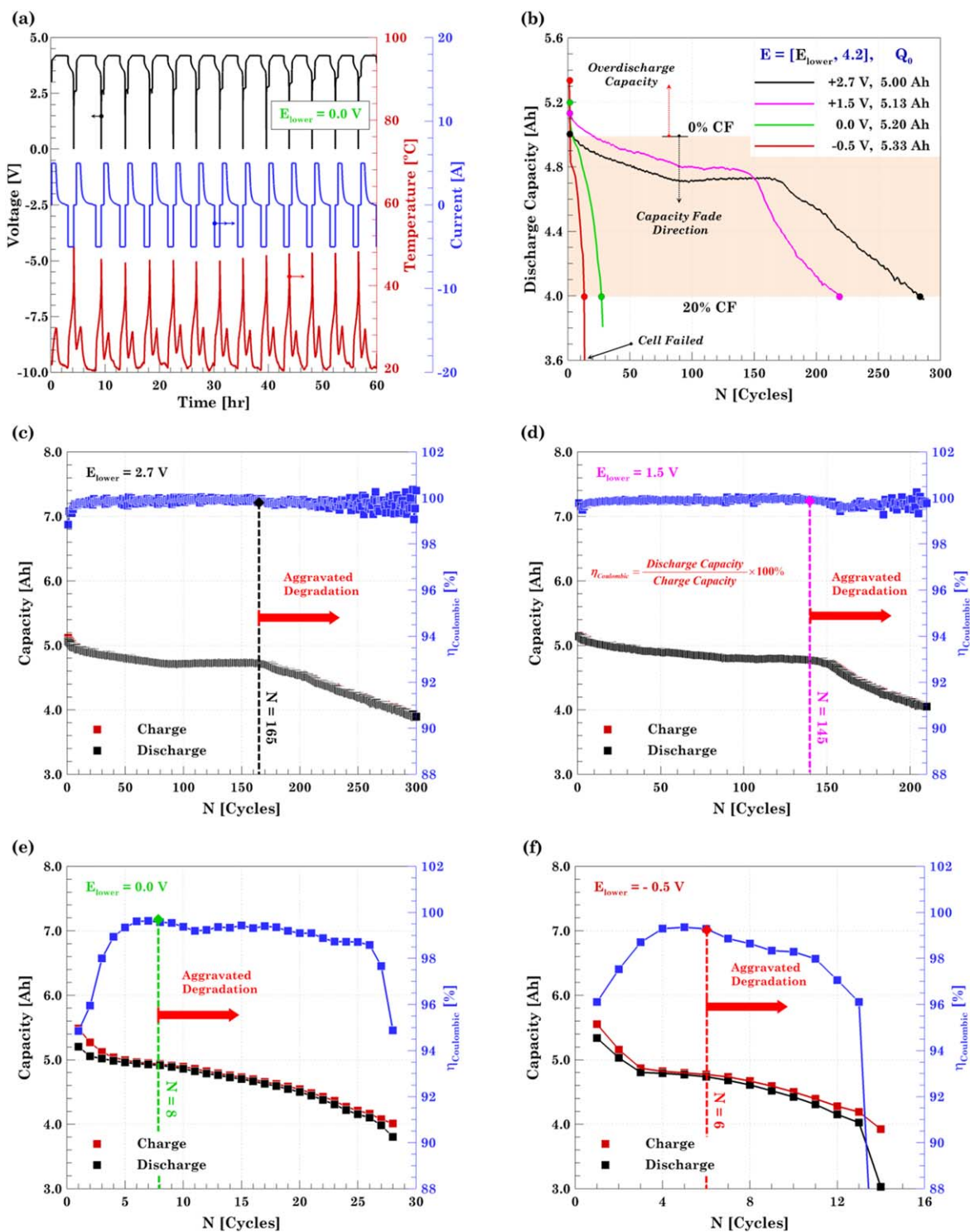


**Figure 2.** Long-term performance of cells aged under different overdischarge conditions. (a) Representative cycling protocol corresponding to the cell aged under the onset of the reverse potential condition,  $E = [0.0, 4.2]$  V. (b) Cycle life comparison based on the discharge capacity. Capacity and coulombic efficiency for (c) aging dominated case, 2.7 V; (d) slight overdischarge case, 1.5 V; (e) reverse potential onset case, 0.0 V; and (f) deep overdischarge case,  $-0.5$  V.

the cycling life. Meanwhile, the discharge IR shows a significant increment at the beginning of the test which depends on the extent of the overdischarge and decreases as the cell ages due to the Cu migration from anode to cathode. Two facts can be inferred from Figs. 4a–4d. First, that the IR value depends not only on the SOC but also on the extent of the cutoff voltages; and second, that the IR does not always increase significantly with aging.

Based on both IR values, a third SoH estimator,  $\Phi_R$ , defined by Eq. 1, is calculated and shown in Figs. 4a–4d. At the beginning of the aging test, the cells cycled in the safe voltage window satisfy the condition that  $R_{\text{Int,D}} > R_{\text{Int,C}}$  and consequently  $\Phi_R < 0$ . Defining  $\Phi_R = 0$  as the onset of aggravated degradation makes sense if the cells are overcharged since  $R_{\text{Int,C}}$  increases faster than  $R_{\text{Int,D}}$  and at some point  $R_{\text{Int,C}} > R_{\text{Int,D}}$ .<sup>27</sup> For the overdischarged cells, 0.0 and

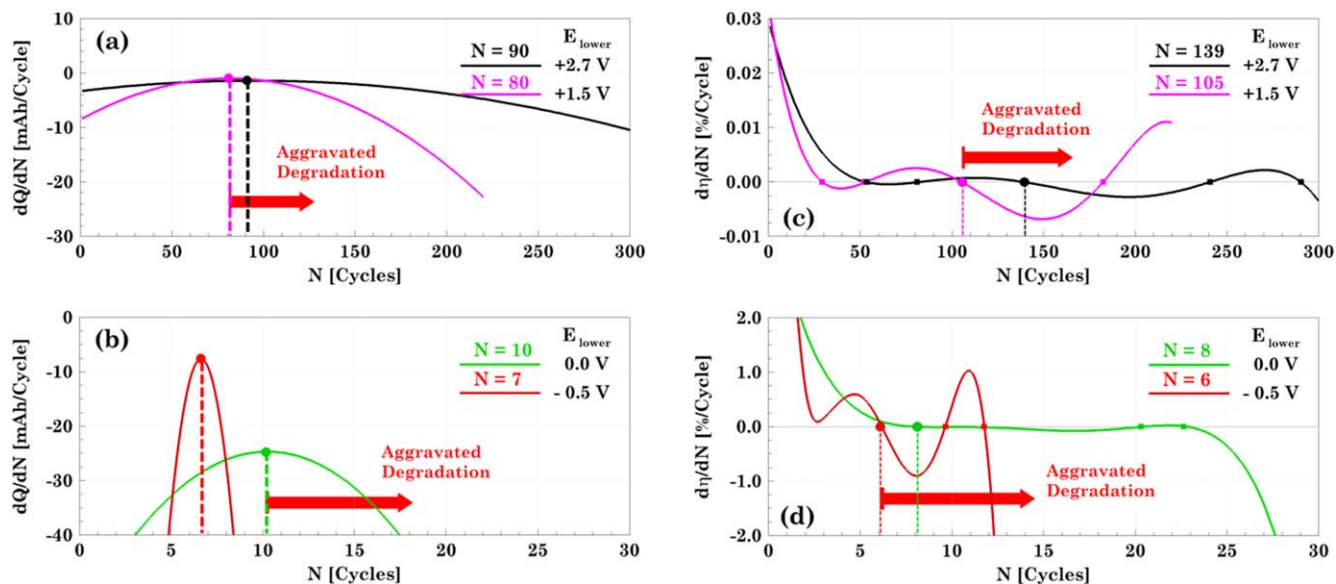


**Figure 3.** (a), (b) Differential capacity and (c), (d) differential coulombic efficiency for the cycle life of the cells aged under overdischarge conditions. The inflection points on the differential capacity can be interpreted as the onset of fast degradation. The cycle where aggravated degradation takes place is the closest one to the cycle indicated in Fig. 2. The maximum coulombic efficiency, represented by the zeros, is used as a SoH indicator.

$-0.5$  V,  $R_{\text{Int,D}} \gg R_{\text{Int,C}}$ , then  $\Phi_R \ll 0$ . Even if the cell is degrading at a faster rate,  $\Phi_R$  may not be necessarily zero, Figs. 4c–4d, and it cannot be used to estimate as a reference. Instead, the trough from the  $\Phi_R$  curve represents the onset of aggravated degradation in Figs. 4a–4b. After this point,  $\Phi_R$  rises at a faster rate because the cell degradation increases  $R_{\text{Int,C}}$ . The indicated cycle in Figs. 4c–4d is selected based on the point where  $\Phi_R$  increases drastically due to a drop in  $R_{\text{Int,D}}$ . The three SoH indicators are compared in Fig. 4e. Predictions made with  $\Phi_R$  approximates better to the actual degradation onset, especially for the 2.7 and 1.5 V cells. For the cells aged under reversal conditions, all three predictors,  $dQ/dN$ ,  $d\eta/dN$ , and  $\Phi_R$  are close to the actual point of failure.

The cycle predictions made with the degradation number,  $\Phi_R$ , are taken as a reference to further inspect the electrochemical, Fig. 5, and thermal, Fig. 6, variations throughout cycling. Voltage and temperature profiles are provided for five cycles corresponding to the first cycle (0% CF), last cycle (20% CF), and the cycle where faster degradation starts ( $\Phi_R$  prediction), and two more cycles in between those three points.

Charge and discharge voltage profiles for the four cells under analysis are shown in Figs. 5a–5d. The discharge curves show how the capacity slowly decreases before the predicted  $\Phi_R$  cycle is reached. Once the cell crosses this cycle the capacity reduces at a faster rate. For instance, the 1.5 V cell takes 131 cycles to reduce its capacity from 5.12 to 4.78 Ah, Fig. 5b. When the degradation accelerates, it takes only 89 cycles to reduce its capacity from 4.78 to 3.97 Ah. Cycling the cell under reversal condition, as in the 0.0 and  $-0.5$  V cells, significantly increases the CF rate, Figs. 5c–5d. For instance, the  $-0.5$  V cell takes only 14 cycles to reduce its capacity from 4.80 to 3.02 Ah. A comparison between the charge/discharge curves from the 2.7 and the  $-0.5$  V cells do not show any significant difference. Only the discharge curve for the last cycle (3.02 Ah) from the  $-0.5$  V cell exhibits a slight change in trend at the end of the discharge. The fast voltage decay is mainly due to the fast anode potential rise and the decomposition of the SEI layer.

The differential voltage ( $dV/dQ$ ) curves from Figs. 5e–5h are obtained by differentiating the 7th order polynomial fitting curves associated with each of the voltage curves. The  $dV/dQ$  peaks can be interpreted in two different ways; either as the transition between phases in the electrodes or as the temporal variation of the resistance as a function of the SOC. The results for charge and discharge are

shown in a mirrored way for ease of interpretation of the plots. From the phase transition point of view, the  $dV/dQ$  peaks correspond to the phase transitions occurring in graphite throughout the charge/discharge process.<sup>35</sup> The small peaks from the cell discharged to 2.7 V, indicate a slow phase transition, Fig. 5e. As the cell ages, the peak intensity increases (vertical slippage) due to a non-uniform lithiation and a simultaneous presence of multiple phases. The most representative feature of the aging phenomena is the horizontal slippage of the peaks.<sup>36,37</sup> The slippage magnitude increases with the extent of the lower cutoff voltage, Figs. 5g–5h. A comparison of the  $dV/dQ$  curves between the charge and discharge process confirms the fact that the side reactions only take place during overdischarge, i.e., no matter the lower cutoff voltage, the  $dV/dQ$  plots for charging are similar, Figs. 5e–5h. The  $dV/dQ$  plots also represent the temporal variation of the IR. At the two fully charged and fully discharged conditions,  $|dV/dQ|$  becomes larger confirming the fact that the internal resistance is larger at these two extremes. The magnitude of the internal resistance increases as the cell ages, particularly at the end of the cycle life due to the SEI decomposition/reformation and copper dissolution/deposition imposed by the overdischarge.

**Thermal response.**—The temperature increment response,  $T_{\text{cell}} - T_{\text{inf}}$ , for the charge/discharge curves shown in Figs. 5a–5d is used to estimate the heat generation, Figs. 5e–5h, for the charge/discharge process. It is observed that the temperature increase during discharge is always greater than the charge one. The temperature gap arises from the fact that entropic heat is endothermic at the end of charge and exothermic during discharge. The irreversible heat, on the other hand, is always exothermic for both cases. During the CV charge, temperature drops as a consequence of the decaying applied current.

The maximum temperature observed for the cells discharged to 2.7 and 1.5 V cells in the first cycle of the aging test are 21.6 °C and 18.5 °C, respectively, Figs. 6a–6b. The temperature observed for the cell aged under the onset of reversal potential is 41.0 °C but this temperature is observed in the last cycle Fig. 6c. As the cell is driven into a continuous reversal condition, the gases released due to the electrolyte decomposition increases the internal pressure and causes cell swelling and an additional temperature increment. Swelling not only affects the pouch but also the electrodes/separator assembly configuration. In the cell discharged to  $-0.5$  V, the movement or

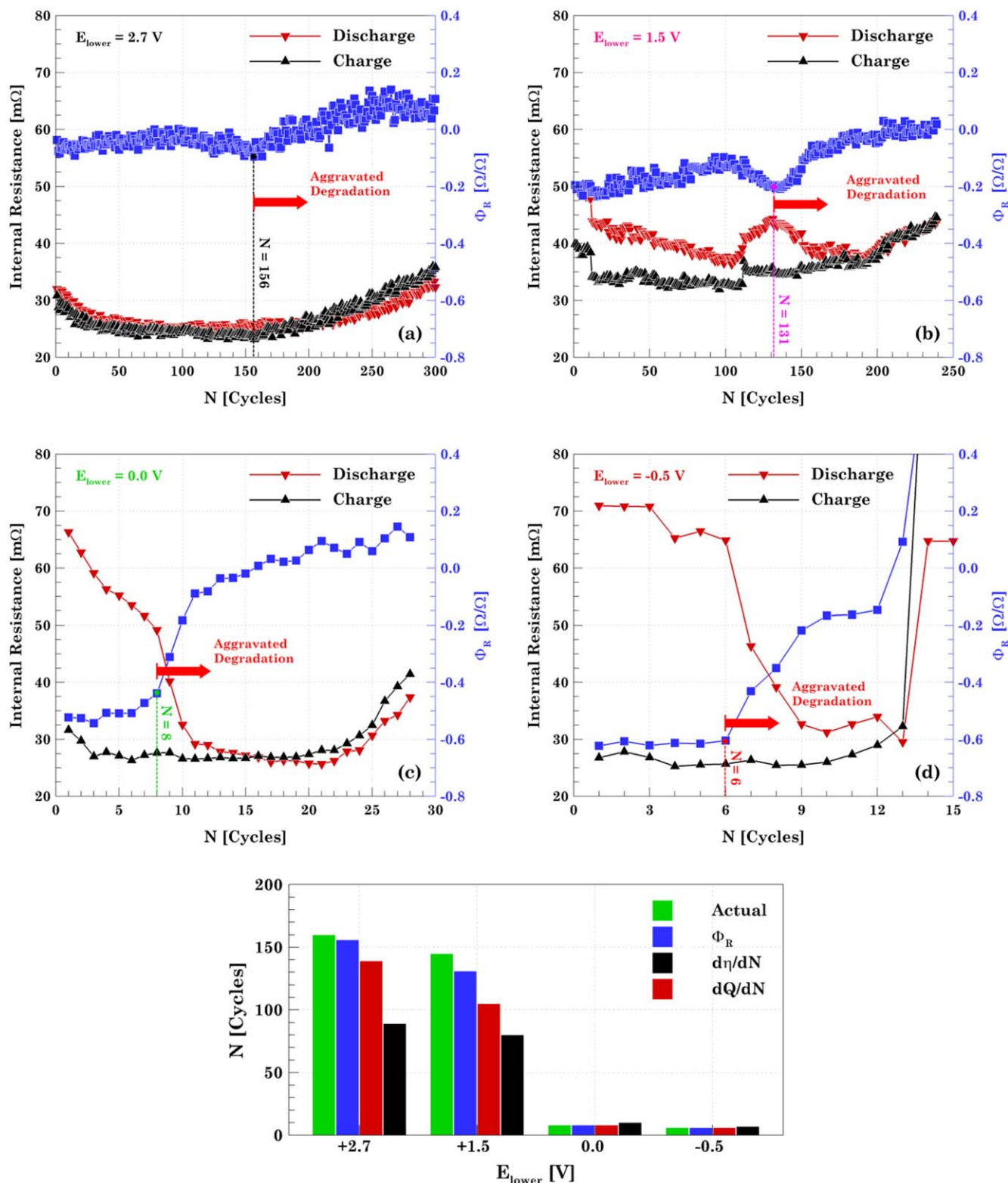


**Figure 4.** Charge/discharge internal resistance evolution with cycling and degradation number for the cells aged at different overdischarged levels,  $E_{lower} =$  (a) 2.7 V, (b) 1.5 V, (c) 0.0 V, and (d) -0.5 V. Extending down the lower cutoff voltage increases the IR at the end of the discharge process, while the IR at the end of the charge remains constant. Accelerated degradation occurs when  $\Phi_R$  increases at a faster rate.

separation of the electrodes internally may have also caused an internal short circuit due to contact between the cathode and anode electrodes. The temperature recorded on the surface of the cell shows a maximum temperature of to 106.0 °C corresponding to a

temperature increase of 83.63 °C, Fig. 6d. Once again, the maximum temperature observed occurs in the last cycle. The thermal results imply that if the cell is cycled above the onset of reversal potential, the maximum temperature will occur in the first cycle when both

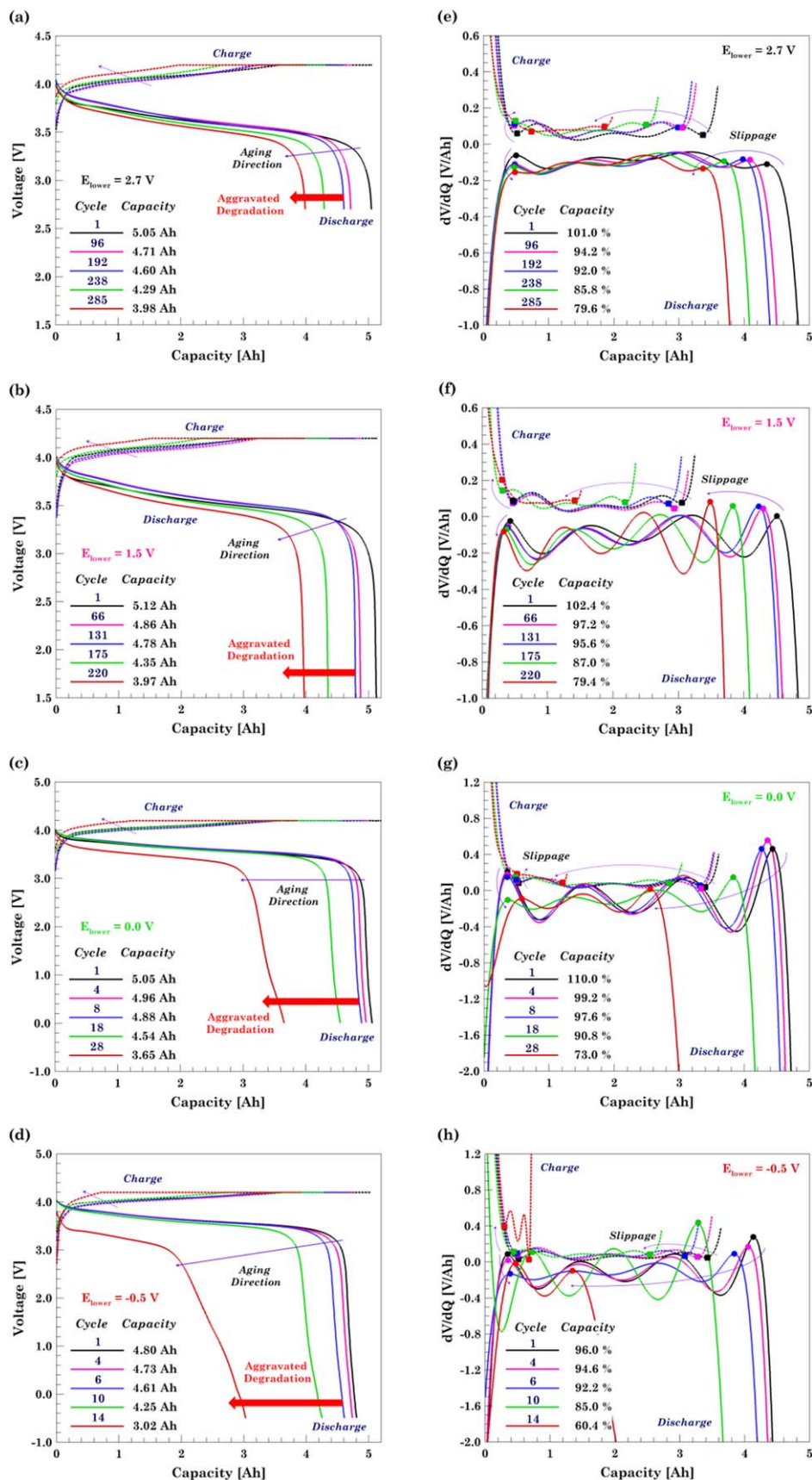


**Figure 5.** Charge/discharge voltage profiles at different degradation levels for the (a) aging dominated case, 2.7 V; (b) slight overdischarge case, 1.5 V; (c) reverse potential onset case, 0.0 V; and (d) deep overdischarge case, -0.5 V. Differential voltage curves are obtained by differentiating the 7th order polynomial fitting curves associated to the each of the voltage curves. Horizontal peaks slippage in the differential voltage curves indicates the capacity loss rate.

active materials are available for reacting. However, if the cell is cycled near or to a reversal condition, then degradation and side reactions will be the ones leading the temperature rise.

In order to complement the thermal analysis, heat generation plots are estimated from an inverse heat transfer problem using the ambient and cell temperature profiles, Figs. 6e–6h. A comparison

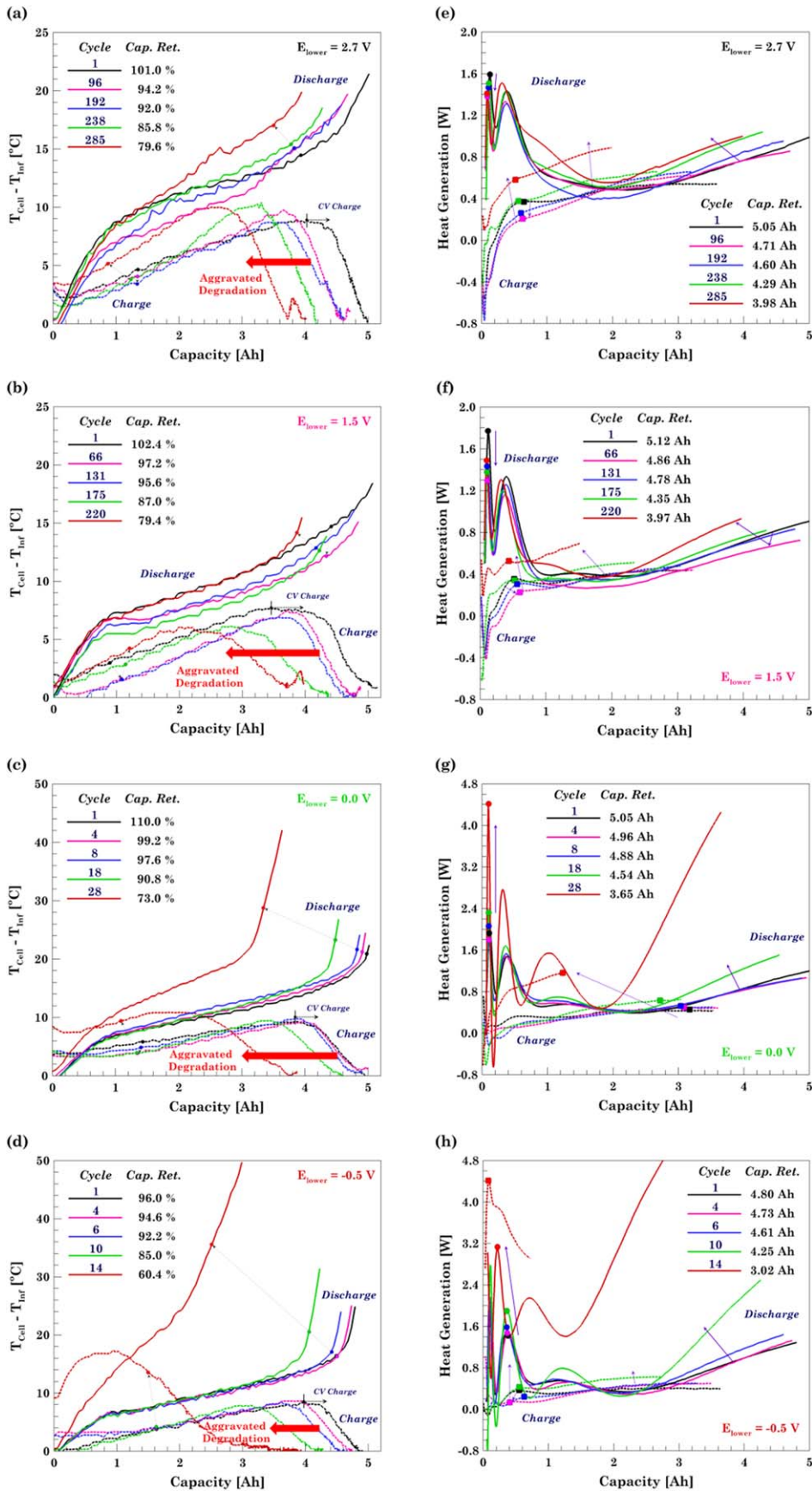


**Figure 6.** Temperature profiles for the charge/discharge process at different degradation levels for the (a) aging dominated case, 2.7 V; (b) slight overdischarge case, 1.5 V; (c) reverse potential onset case, 0.0 V; and (d) deep overdischarge case, -0.5 V. Heat generation curves are obtained via an inverse heat transfer method. The maximum temperature during both, the charge and discharge processes, increases as the cell ages and it aggravates by decreasing the lower cutoff voltage. Horizontal peaks slippage indicates capacity loss with cycling and vertical slippage represents the degradation effect on the cell.

between the  $dV/dQ$  and heat generation plots exhibits some similarities. The link between both results is internal resistance. One of the major contributors to irreversible heat is the Joule heating ( $i^2R_{int}$ ), which depends on the current applied and internal resistance of the cell. During the charging process, the heat generated remains quasi-constant because the internal resistance does not change. In the case of the discharge process for the 2.7 and 1.5 V cells, the maximum heat generated occurs at the beginning of the discharge and its magnitude decreases as the cell ages, Figs. 6e–6f. A similar trend is found in the cells aged under reversal condition, Figs. 6g–6h; however, this time the heat generated becomes steeper at the end of the discharge. This implies that the additional degradation

mode such as SEI and electrolyte decomposition and excessive copper dissolution are the causes behind the rapid temperature rise.

**DPA.**—The thermal and electrochemical results can be supported by a physical inspection of the cell components. Figures 7a–7d shows the final condition of the four cells after their capacity faded by 20%. Since the 2.7 V cell did not swell, it is not included in this figure. As the lower voltage is extended, the cell volume expansion becomes more severe, indicating gas generation from the decomposition of the electrolyte and the LCO electrode,<sup>38</sup> Figs. 7a–7b. In the case of the –0.5 V cell, a small charring spot can be observed on the left side of the pouch from Fig. 7c. The continuous cycling under reversal

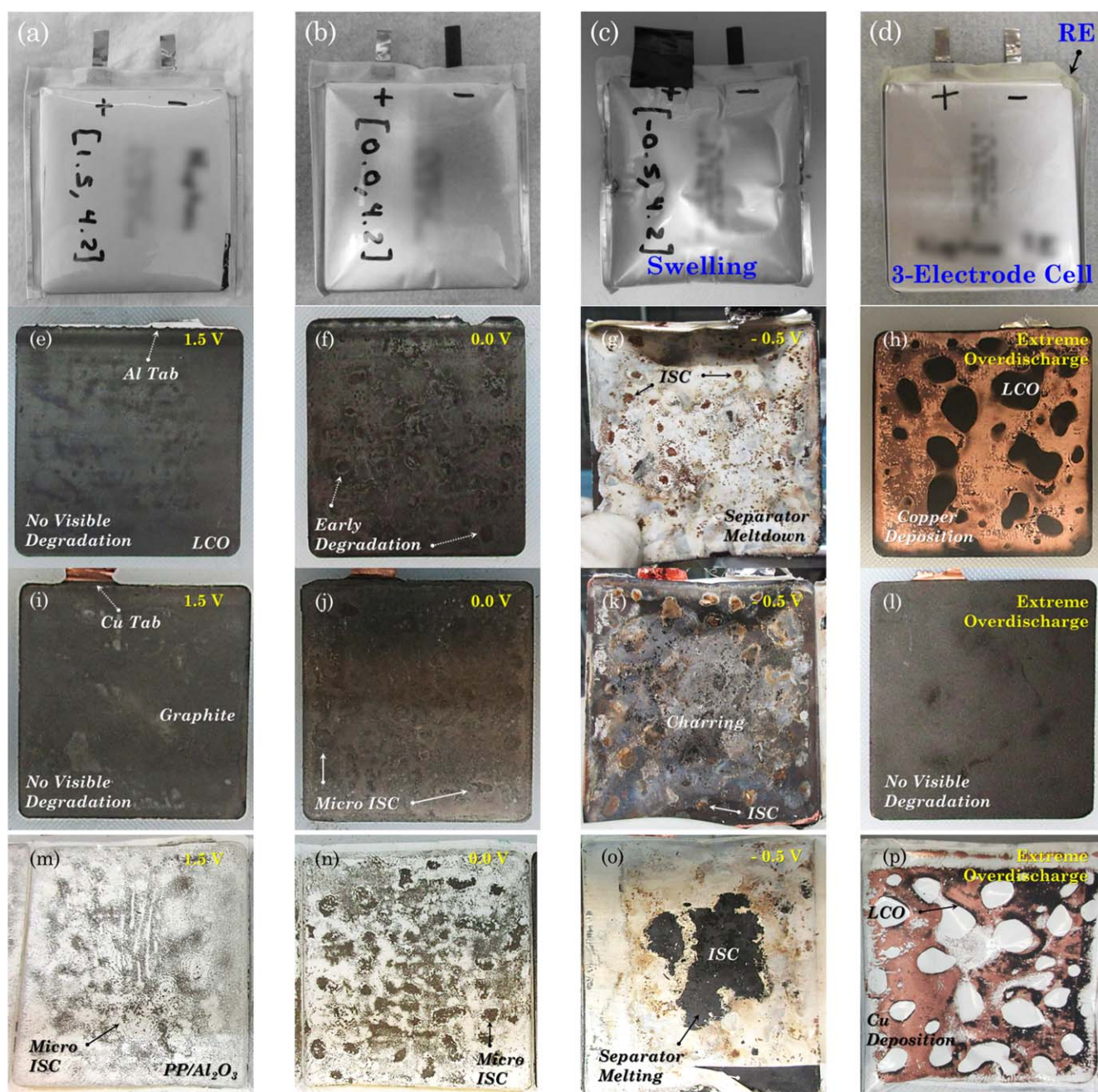


**Figure 7.** Destructive physical analysis under overdischarge condition at the end of the cycle life. (a)–(c) Cell condition prior to conducting the DPA test. (d) The extremely overdischarged three-electrode cell is included as a reference for the DPA analysis. (e)–(g) LCO and (i)–(l) graphite electrodes, and (m)–(p) separator samples retrieved after cell autopsy.

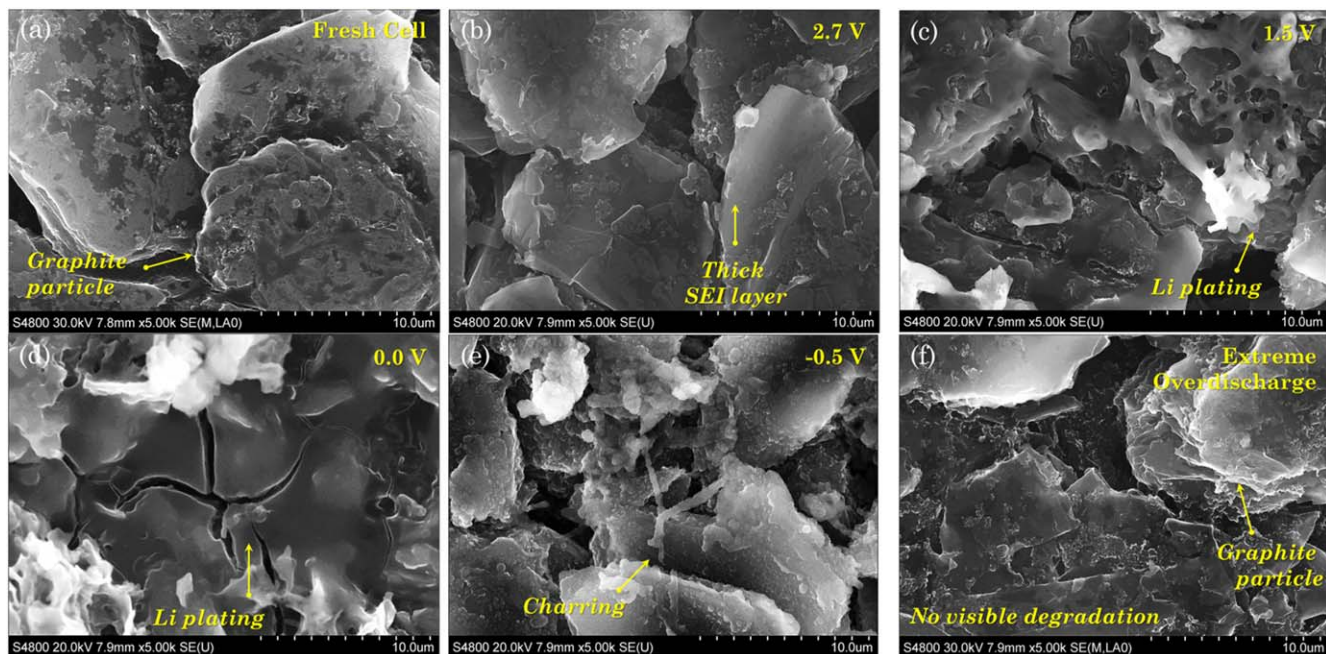


**Figure 8.** Micrographs of graphite electrode samples extracted from aged cells at different lower cutoff voltages. (a) Pristine electrode. (b) Aging dominated case characterizes by SEI growth. (c) Slight overdischarge case characterizes by Li plating presence and further SEI thickening. (d) The onset of reverse potential case exhibits different morphologies of Li-plating covering the electrode surface. (e) Deep overdischarge case exhibits charring on the particle surface caused by ISC. (f) The extreme overdischarge electrode only shows the graphite particles without any deposits or evidence of the SEI layer. Scale bar for all images is 10  $\mu\text{m}$ .

condition leads to repeated breakdown and reformation of the SEI layer, decomposition of the electrolyte, dissolution of copper and delamination of the anode, all of which lead to the generation of the gases that expand the cell. The gas buildup creates a bubbling effect that causes physical separation between the electrodes and deformation of the electrodes/separator assembly. The formation of copper and lithium bridges between electrodes leads to an internal short circuit, which heats the cell internally. Even though the temperature ramps up to 106.0  $^{\circ}\text{C}$ , the cell did not go into thermal runaway. The cell vented through the left and right edges, causing the charred spot and dent in its center. The results from the extremely overdischarged three-electrode cell is also included as part of the analysis, Fig. 7d, to understand the difference between repeated overdischarge of a cell and a one-time extreme overdischarge. Even though the extremely overdischarged cell is dead at the end of the test, no evidence of swelling is found, since the decomposed SEI layer is never re-formed. This highlights the important point that overdischarge is a benign abuse condition by itself but can turn into a problem when combined with subsequent charging. The interplay between the degradation mechanisms of aging and overdischarge poses a threat to cell integrity and operator health.

Since the cell has 23 double-side coated layers for each of the electrodes as well as two separators, hence it would be impractical to include the whole set of photographic evidence. Instead, a representative sample from the LCO cathode, Figs. 7e–7h; graphite anode, Figs. 7i–7l; and separator, Figs. 7m–7p, are included here. Before analyzing the aged cells, the components of the three-electrode cell that underwent extreme overdischarge were inspected to establish a baseline for the condition where overdischarge dominates. As the cell is overdischarged, the graphite anode is excessively de-lithiated until the lithium inventory depletes. Then SEI starts decomposing in order to donate more electrons, which reduces  $\text{Li}^+$  ions present in the electrolyte at the LCO cathode.<sup>39</sup> When the anode potential exceeds  $\sim 3.54\text{ V}$  vs  $\text{Li}/\text{Li}^+$ , the Cu current collector starts oxidizing and the Cu-ions start migrating to the cathode and they deposit on the surfaces of the cathode and

separator.<sup>17,40</sup> Copper deposition, with its characteristic bronze color, can be observed on the LCO electrode and separator from Figs. 7h and 7p, respectively. The graphite electrode of the extremely overdischarged cell resembles the graphite electrode that was discharged to the normal discharge voltage, Fig. 7l. In the extremely overdischarged case, Fig. 7e, the cell is not able to be charged again because copper deposition internally shorts the cell.

In the case of the aged cells, no visible degradation is found on any of the electrodes for the 1.5 V cells, Figs. 7e–7i, only the separator exhibits some brownish spots mostly due to micro-shorts caused by sparse Li plating spots. For the 0.0 V cell, more micro-shorts are observed on all the three components, Figs. 7f, 7j, 7n. The idea that overdischarge promotes the formation of Li plating may sound counterintuitive, since Li deposition occurs during charging. However, the degradation imposed by the overdischarge process increases the cell IR and during the charging process, the increased overpotential can drive the anode potential below zero and promote Li plating.<sup>41</sup> In the case of the cell aged under reversal condition,  $-0.5\text{ V}$  cell, the deposition of copper on the cathode and separator electrochemically blocks the graphite electrode during the overdischarge process. During charge, the blocked cathode produces uneven lithiation of the anode and, with the continuous cycling, lithium plating eventually takes place. The combination of Cu on the cathode surface and Li metal on the anode short circuited the cell. Internal short circuits become so severe in the  $-0.5\text{ V}$  cell that it causes charring on the graphite electrode, Fig. 7k, and separator meltdown, especially around the center of the cell, Fig. 7o. After the polypropylene from the separator melts, it sticks to the LCO electrodes making it hard to separate the electrode from the separator, Figs. 7g, 7o.

**SEM/EDS.**—The actual degradation on the cell components is further investigated by extracting representative samples and analyzing their morphology, Figs. 8–10, and composition, Tables I and II. The morphology of the fresh graphite electrode is shown in Fig. 8a. Prior to any cycling, the inner layers from the platelet

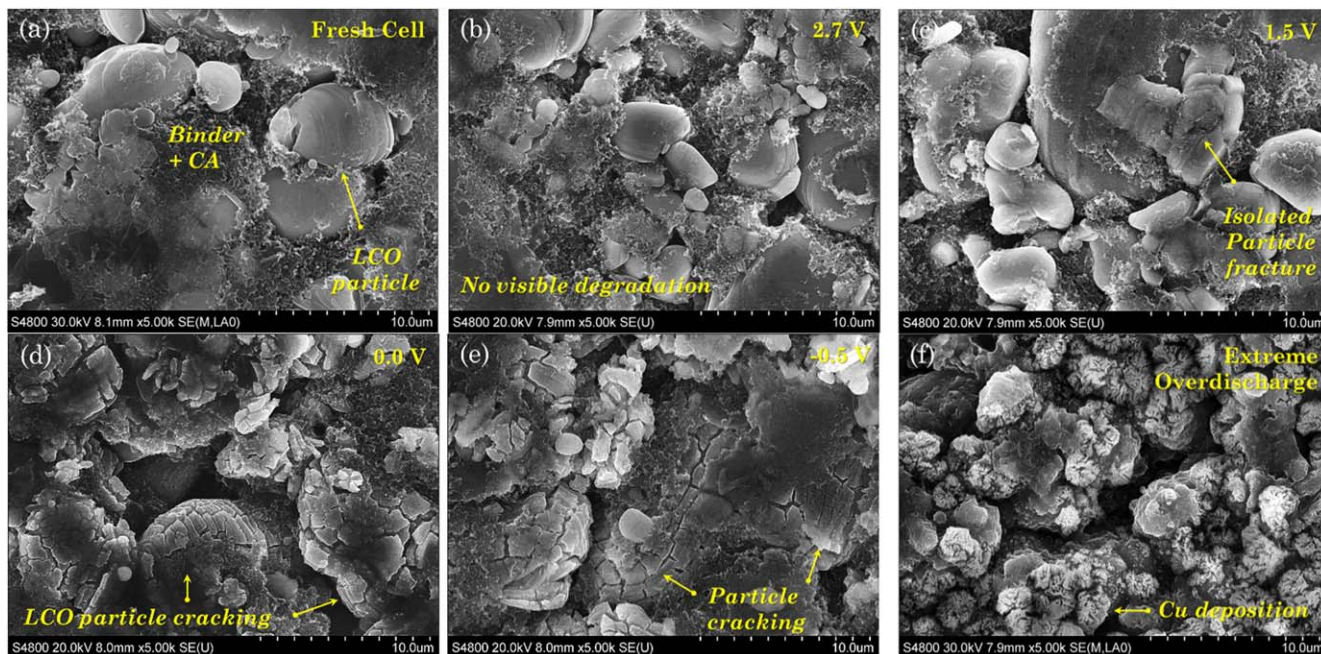


**Figure 9.** Micrographs of LCO electrode samples extracted from aged cells at different lower cutoff voltages. No evidence of fracture is found in the samples corresponding to the (a) pristine electrode and the (b) aging dominated case cell. (c) Slight overdischarge case shows sparse LCO particles with an early presence of fracture. (d)–(e) LCO particle cracking predominantly happen in the cells overdischarge under reversal condition due to electrochemical soaking. (f) The LCO electrode from the extreme overdischarge cell exhibited the characteristic Cu deposition on its surface. Scale bar for all images is 10  $\mu\text{m}$ .

**Table I.** Electrodes composition extracted from the EDS test of graphite and LCO electrodes at different overdischarge voltages for the samples shown in Figs. 8 and 9<sup>a</sup>.

$E_{\text{lower}}$ [V]	Anode							Cathode						
	C	O	F	Al	P	Cu	Co	C	O	F	Al	P	Cu	Co
FC	95.9	0.0	1.8	1.4	0.9	0.0	0.0	31.9	18.7	5.3	4.0	0.0	0.0	40.1
2.7	76.4	18.5	3.2	1.4	0.5	0.0	0.0	31.3	18.8	6.8	5.3	0.3	0.0	37.5
1.5	69.2	25.2	3.9	0.8	0.7	0.0	0.2	31.5	19.4	8.3	2.5	0.8	0.0	37.4
0.0	48.6	39.6	8.5	1.2	1.2	0.9	0.1	36.4	22.8	10.2	1.9	0.5	0.0	28.1
−0.5	71.4	12.1	14.4	0.6	0.9	0.6	0.0	34.4	24.7	9.8	2.1	1.0	0.1	27.9
EO	86.1	0.0	8.3	1.7	1.6	2.3	0.0	0.0	11.3	1.7	14.6	0.3	64.1	8.0

a) The values listed correspond to the wt. % of each element found in the samples.

graphite particle are well defined. The electrode composition is mostly carbon from the active particle and the conductive additive. The presence of aluminum comes from the ceramic coating from the separator, Table I. Once lithium intercalates/de-intercalates during normal cycling, the interspaces get covered with a thin SEI film that becomes thicker with aging, Fig. 8b. The SEI layer consists of a mixture of different compounds such as lithium fluoride (LiF), lithium hydroxide (LiOH), lithium carbonate ( $\text{Li}_2\text{CO}_3$ ), lithium oxide ( $\text{Li}_2\text{O}$ ), and lithium alkyl carbonate ( $\text{ROCO}_2\text{Li}$ ,  $\text{RCOLi}$ ).<sup>42</sup> The formation of these compounds increases the oxygen and fluorine content and reduces the carbon percentage. For the cell that was subjected to continuous discharges down to 1.5 V, dendrites populate the electrode surface. Even though the EDS cannot detect small elements like hydrogen or lithium, the presence of lithium can be confirmed when the highly reactive nature of lithium leads to the formation of lithium oxide when it reacts with the oxygen from the air. Thus, the Li plating increases the oxygen content and reduces the carbon content as shown in Table I. The small percentage of cobalt on the graphite electrode indicates that there is a minor cobalt migration from cathode to anode during the charging process. As the lower voltage is decreased to 0.0 V, lithium plating and SEI growth

aggravate, Fig. 8d. The elemental composition of the electrode shows a further increase in its content of oxygen and fluorine and cobalt can still be detected, see Table I. A noteworthy detail from this electrode is the presence of copper. During the initial cycles, the anode potential may not be high enough to dissolve the current collector, but as the cell ages and the internal resistance increases, the Cu current collector starts dissolving. The simultaneous presence of Cu deposition and Li plating increases the likelihood of triggering an internal short. In the cell aged under reversal condition, the cumulative effect of all the degradation mechanisms are observed, such as the formation of gases, cell swelling, and internal short circuit. In the case of the cell discharged in continuous cycles to −0.5 V the electrode surface is observed to be covered with residuals of charring and melted separator, as shown in Fig. 8e. Charring increases the carbon content; and the SEI decomposition reduces the oxygen content, see Table I. Finally, the graphite electrode from the extremely overdischarged cell shows a similar morphology to the fresh cell. In fact, the absence of intercalated lithium, melted separator, and copper makes the inner layers of the graphite particle more distinguishable. In terms of the composition, the extremely overdischarged anode has similar carbon content to

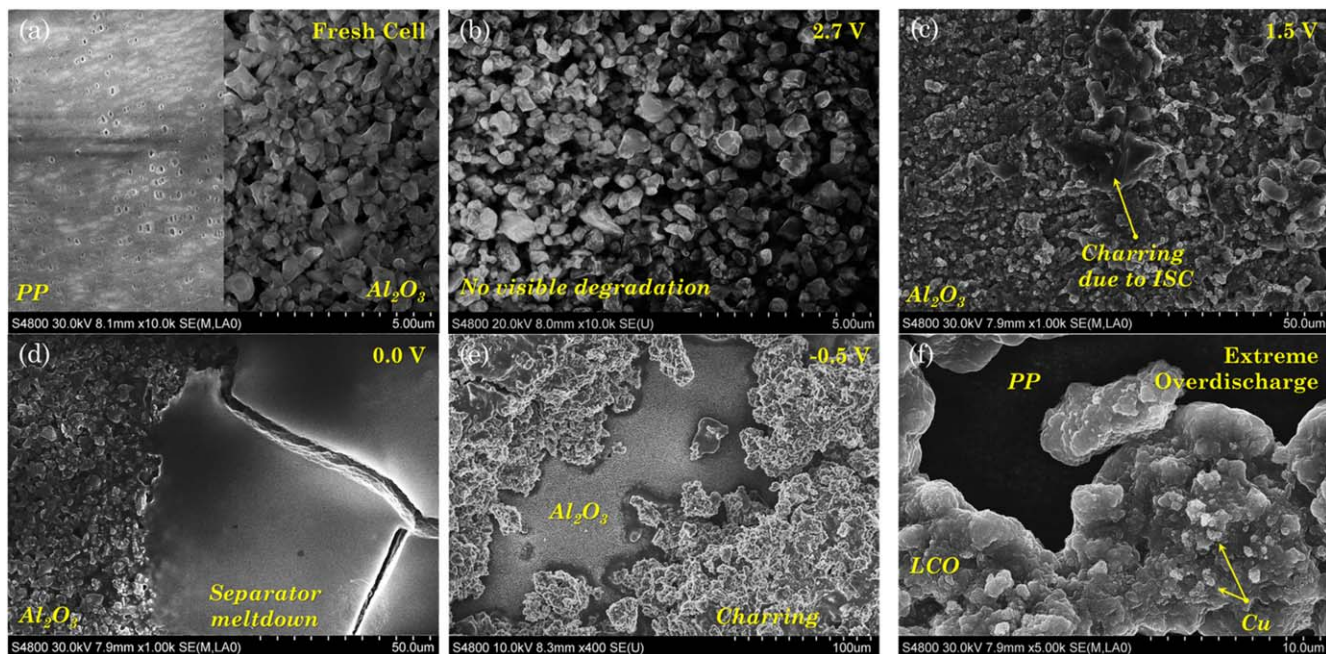


**Figure 10.** Micrographs of separator samples extracted from aged cells at different cutoff voltages. (a) The separator is made of PP with  $\text{Al}_2\text{O}_3$  ceramic layer. The PP side is facing the LCO electrode while the  $\text{Al}_2\text{O}_3$  is facing the graphite one. (b) Aging dominated case separator shows no evidence of degradation. (c) Slight overdischarge case exhibits some deposits in the ceramic layer due to ISC. (d) The onset of reverse potential case exhibits a larger presence of deposits mainly on the  $\text{Al}_2\text{O}_3$  layer. (e) The intensive ISC from the cell aged under the deep overdischarge condition induces charring and separator meltdown. (f) The extreme overdischarge cell did not show any significant degradation on the  $\text{Al}_2\text{O}_3$  side but it did show LCO incrustations with Cu deposited on it. The scale bar is different on each panel to enhance the representative degradation details.

**Table II. Electrodes composition extracted from the EDS test of separator at different overdischarge voltages for the samples shown in Fig. 10<sup>9)</sup>.**

$E_{\text{lower}}$ [V]	Separator						
	C	O	F	Al	P	Cu	Co
FC	0.0	41.2	9.5	47.9	1.3	0.0	0.0
2.7	8.8	43.9	1.5	45.1	0.6	0.0	0.1
1.5	27.1	37.8	3.4	28.1	1.3	0.0	2.3
0.0	7.0	50.4	3.1	38.6	0.8	0.0	0.2
-0.5	27.4	58.0	8.5	4.6	1.1	0.2	0.2
EO	0.0	21.2	7.3	17.3	2.4	24.9	26.9

a) The values listed correspond to the wt. % of each element found in the samples.

that of the fresh cell, and as expected there is a presence of Cu from the current collector but there is no oxygen. The result supports the idea that when the anode lithium inventory gets depleted, the SEI decomposes to fulfill the power demanded by the external load.

The morphology of a fresh cathode is shown in Fig. 9a. Its composition confirms LCO is the active material and it has an aluminum current collector. In this figure, the LCO active particle and the secondary phase (binder and conductive additive) are well defined. If the cell is aged under normal conditions, Fig. 9b, no significant change in the morphology and composition, Table I, is observed in the micrograph and the EDS results, respectively. Sparse spots with cracked LCO particles are found when the cell is slightly overdischarged, Fig. 9c. Severe LCO particle cracking occurs when the cells are cycled down to 0.0 and -0.5 V due to over-lithiation of the cathode, Figs. 9d-9e. In other words, under normal discharge conditions, Li-ions migrate from anode to cathode to occupy one of the available and relevant parent sites of LCO. However, if the cell is extremely overdischarged, the LCO particle is not able to allocate all

the  $\text{Li}^+$  ions being reduced from the electrolyte to the relevant Li layer in the octahedral structure. Therefore, the active particle starts swelling and with continuous cycling, it eventually cracks.<sup>43</sup> The structural disintegration of the LCO particles not only increases the transport resistance in the solid phase but also reduces the capacity retention.<sup>40,44</sup> In terms of the composition, the Co content decreases as the end-of-discharge voltage decreases. Particle cracking exposes the interior of the LCO particles and raises the oxygen content. Finally, the LCO electrode, from the extremely overdischarged cell, exhibits the deposition of copper onto its surface, Fig. 9f. The Cu deposits hinders the complete detection of the LCO electrode when the composition is estimated. The separator from this cell is made of PP facing the LCO electrode and alumina coating facing the graphite electrode, Fig. 10a. The composition indicated in Table II corresponds to the alumina side. The polypropylene,  $(\text{C}_3\text{H}_6)_n$ , side of the separator only shows carbon content. In the case of the 2.7 V cell, no significant change with respect to the separator is found, Fig. 10b, except for the small presence of carbon and cobalt. Micro-shorts become visible in cell discharged to 1.5 V, in the form of deposits on the alumina side, Fig. 10c, and it's more evident on the cell discharged to 0.0 V, Fig. 10d. The deposits coming from the anode contains SEI and Li plating residuals that increase the oxygen content and reduce the Al percentage. In the case of the cell discharged to -0.5 V, Fig. 10e, the high temperature caused by the internal short causes charring on the graphite electrode and the heat produced causes the electrode active material to stick to the separator. Charring residuals increase the carbon content and significantly reduce the Al content. One of the most significant results is the presence of copper in the separator. In general, internal short circuits are more commonly attributed to Li plating; however, if the cell is overdischarged under a reversal condition, then the dissolved Cu can cause internal shorts. One of the main differences between an extreme overdischarge and a continuous overdischarge is reflected on the separator, where the copper dissolved deposits on the cathode and PP separator surface in the latter. During the DPA, the LCO active material detaches from the electrode and sticks onto

the PP separator. This was confirmed by the presence of Co and Cu content on the separator from this cell.

### Conclusions

In this work, the effect of both aging and overdischarge on pouch cells was studied experimentally and analytically. The cells were subjected to cycling under continuous overdischarge condition wherein the lower cutoff voltage is judiciously chosen (2.7, 1.5, 0.0 and  $-0.5$  V) to ensure cyclability of the cell. The electrochemical results showed that the additional capacity gained by extending the lower cutoff voltage is negligible. Even more, the cycle life is compromised, especially if the cell is aged under a reversal condition ( $E_{\text{lower}} \leq 0.0$  V). The SoH of the cells is also investigated via differential capacity and differential coulombic efficiency curves and then compared with a new IR-based SoH parameter. The proposed SoH indicator,  $\Phi_R$ , can predict the onset of aggravated degradation in all cells.

Four long-term cycling conditions are analyzed in order to shed light onto the degradation mechanisms imposed according to the extent of overdischarge. The aging dominated case, 2.7 V, represented the normal aging condition characterized mainly by the SEI thickening. The slight overdischarge case, to 1.5 V, degraded in a similar fashion to the aging dominated one but with an increased presence of Li plating. The reverse potential onset case, to 0.0 V, represented the condition where anode potential becomes larger than the cathode potential. Li plating on the anode, particle cracking on the cathode, and an early dissolution of anode current collector followed by a Cu bridge formation on separator are the main degradation mechanisms behind the short cycle life of the cell. The deep overdischarge case, to  $-0.5$  V, initially exhibited the same degradation mechanisms to the cell discharged to 0.0 V but at the end failed after a few cycles. The disintegration of the LCO particle structure caused by over-lithiation, as well as the repeated SEI breakdown and reformation, electrolyte decomposition, etc. led to the formation of gases. Finally, the formation of copper and lithium bridges led to direct contact between the electrodes resulting in micro-shorts or internal shorts.

Overdischarge is a benign abuse test per se that can turn into a problematic hazard cause when combined with a subsequent charging. The combined effects of the degradation mechanisms from aging and overdischarge pose a threat to cell integrity and user health especially at the end of the cycle life.

### Acknowledgments

Financial support from the Underwriters Laboratories Inc. is gratefully acknowledged. The Birck Nanotechnology Center characterization and analysis facility at Purdue University is acknowledged.

### Appendix

**Postmortem analysis of pouch cells.**—Postmortem analysis is a robust and widely adapted tool used to gain further insights into the failure analysis of a cell. Opening these cells helps in visualizing and characterizing the changes that occurred in the cell components during the test and compare them with that of a fresh cell. A step by step procedure followed for disassembling the pouch cell is described next.

**Step 1. Insulation of tabs.** Prior the destructive physical analysis (DPA), the tabs of the pouch cells are isolated with electrical insulation tape. This is an extra precaution that needs to be taken in order to avoid any case of an external short circuit, see Fig. A-1a.

**Step 2. Preparation of materials.** Sealing bags are used to store the electrodes, separators and other components of the cell. A total of 5 sealing bags, one for each electrode, one for the separator, one for the electrolyte and one for storing the other cell components such as pouch and tabs are labeled based on the things they will house. A glass vial, vial septum, and a vial cap are used to collect the electrolyte of the cell. All the materials, the cell and a media recorder device are transferred to the glovebox.

**Step 3. Disassembly of the pouch.** After transferring the cell inside the glove box, a plastic board is used to disassemble the cell. This is used to avoid contact of tabs with the metallic floor of the glove box. The process starts with piercing the pouch using a stainless-steel scalpel. This initial cut is made near one of the tabs. Extra care should be taken while using the scalpel to avoid any kind of short circuit and hence it is recommended to keep one of the tabs insulated. The cutting process should be done very slowly and with extra care. Once the cut along the width of the cell is complete, a pair of point-tip plastic tweezers is used to pull up the pouch from the center as shown in Fig. A-1b. After the cut along the length, the pouch is pulled off from the cell forming a T-shaped cut, as shown in Fig. A-1c. The pouch is then cut from the bottom exposing the electrodes-separators assembly, see Fig. A-1d.

**Step 4. Removal of tabs.** The pouch remains connected to the cells through the metallic nickel tabs. A pair of scissors is used to cut the tabs, one by one, and separate the pouch and tabs from the cell, see Fig. A-1d. Extra precaution should be taken while cutting the tabs to avoid short circuit.

**Step 5. Disassembly of separator and electrodes.** After removing the tapes on the external separator, the electrodes-separator assembly can be unwound. Two separate pairs of plastic tweezers are used to extract cathode and anode. Extra care must be taken while separating the electrodes because the electrodes or the active material on the separator may get in contact with other electrode resulting in a short circuit. An image of unwinding the separator and extraction of electrodes is shown in Fig. A-1e.

**Step 6. Electrolyte collection.** The electrodes from commercial cells are typically soaked rather than flooded with the electrolyte. The electrolyte can be collected by rinsing isopropyl alcohol (IPA) over the disassembled pouch, see Fig. A-1e. The mixture is then carefully poured into the glass vial without spilling any of it. The glass vial is then closed with a septum and cap. As IPA is volatile in nature it is important to seal the electrolyte mixture. A manual crimper is used to seal the glass vial. The collected electrolyte is further analyzed to study the decomposition of electrolyte using gas chromatography and mass spectroscopy.

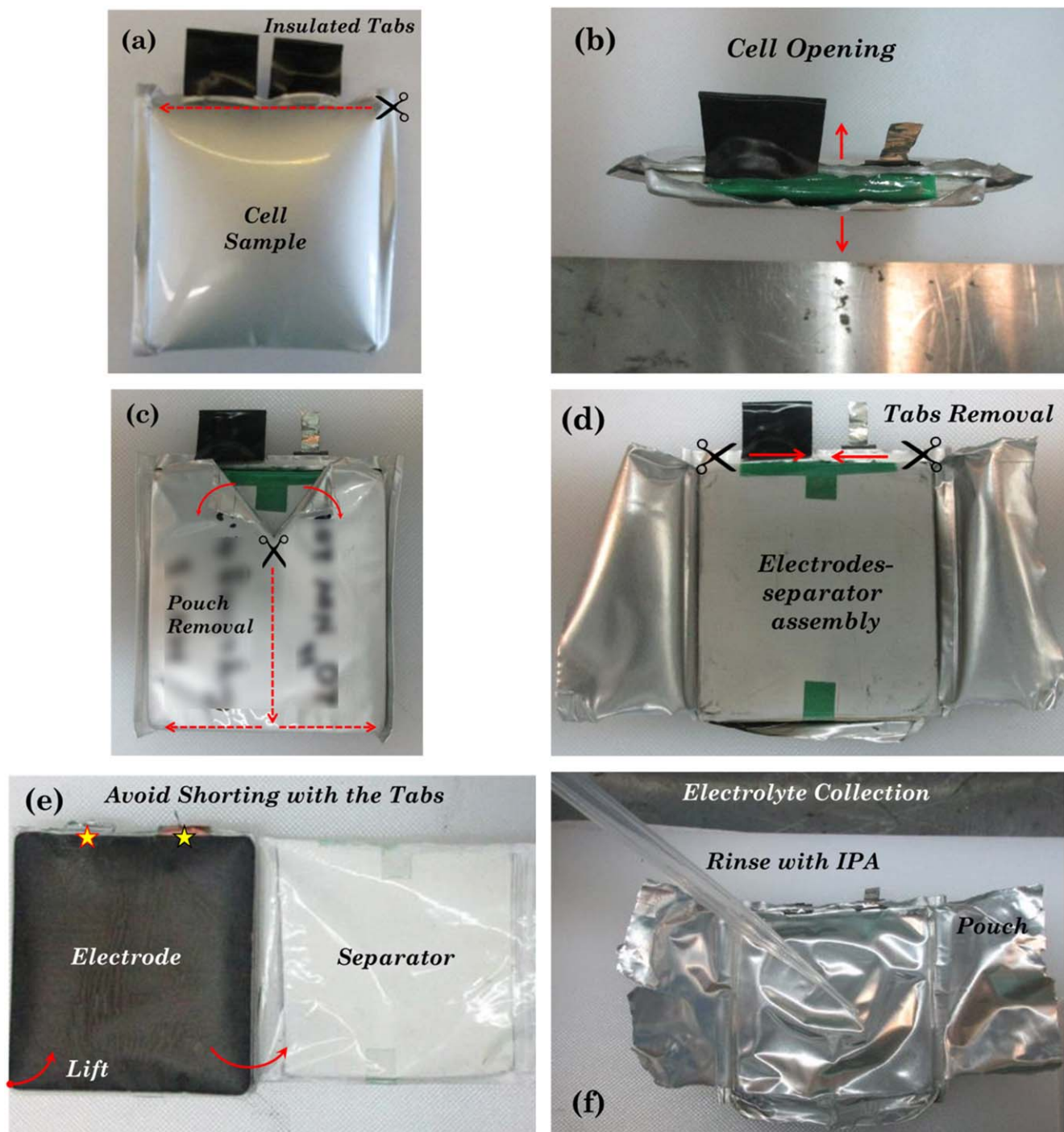


**Figure A-1.** Destructive physical analysis of an aged pouch cell. (a) Isolation of the tabs, (b) cut along the width of the pouch, (c) T-shape cut, (d) cut along the length and bottom of the pouch, (e) unwinding the separator and extraction of electrodes, and (f) IPA poured on the pouch to collect electrolyte.

### ORCID

Daniel Juarez-Robles <https://orcid.org/0000-0003-2746-5775>

Conner Fear <https://orcid.org/0000-0001-6797-3948>

Judith A. Jeevarajan <https://orcid.org/0000-0003-4843-7597>

Partha P. Mukherjee <https://orcid.org/0000-0001-7900-7261>

### References

- M. A. Hannan, M. M. Hoque, A. Hussain, Y. Yusof, and P. J. Ker, *IEEE Access*, **6**, 19362 (2018).
- FAA, "Lithium Batteries & Lithium Battery-Powered Devices." FAA (Federal Aviation Administration) Office of Security and Hazardous Materials Safety, 57 (2018).
- S. Tibken and R. Cheng, Samsung Answers Burning Note 7 Questions, Vows Better Batteries, in *CNET* (2017), Online <https://cnet.com/news/samsung-answers-burning-note-7-questions-vows-better-batteries>.
- U. Irfan, How Lithium Ion Batteries Grounded the Dreamliner, *Tech*, Scientific American (2014), <https://scientificamerican.com/article/how-lithium-ion-batteries-grounded-the-dreamliner/>.
- L. Kong, C. Li, J. Jiang, and M. Pecht, *Energies*, **11**, 2191 (2018).
- T. D. Hatchard, S. Trussler, and J. R. Dahn, *J. Power Sources*, **247**, 821 (2014).
- F. Larsson, S. Bertilsson, M. Furlani, I. Albinsson, and B. E. Mellander, *J. Power Sources*, **373**, 220 (2018).
- F. Larsson and B. E. Mellander, *J. Electrochem. Soc.*, **161**, A1611 (2014).
- L. G. Lu, X. B. Han, J. Q. Li, J. F. Hua, and M. G. Ouyang, *J. Power Sources*, **226**, 272 (2013).

10. F. Baronti, G. Fantechi, R. Roncella, R. Saletti, G. Pede, and F. Vellucci, *2013 IEEE International Symposium on Industrial Electronics (Isie)* (IEEE, Taipei) p. 1 (2013), in Editor.
11. J. A. Jeevarajan, B. Strangways, and T. J. Nelson, Hazards due to overdischarge in lithium-ion cylindrical 18650 cells in multi-cell configurations, National Aeronautics and Space Administration 44th Power Sources (2010).
12. C. F. Lopez, J. A. Jeevarajan, and P. P. Mukherjee, *J. Electrochem. Soc.*, **162**, A1905 (2015).
13. A. Manthiram, *ACS Central Science*, **3**, 1063 (2017).
14. J. Chen, C. Buhrmester, and J. R. Dahn, *Electrochem Solid St*, **8**, A59 (2005).
15. X. Lai, Y. Zheng, L. Zhou, and W. Gao, *Electrochim. Acta*, **278**, 245 (2018).
16. H. Maleki and J. N. Howard, *J. Power Sources*, **160**, 1395 (2006).
17. C. Fear, D. Juarez-Robles, J. A. Jeevarajan, and P. P. Mukherjee, *J. Electrochem. Soc.*, **165**, A1639 (2018).
18. H. He, Y. D. Liu, Q. Liu, Z. F. Li, F. Xu, C. Dun, Y. Ren, M. X. Wang, and J. Xie, *J. Electrochem. Soc.*, **160**, A793 (2013).
19. A. Barré, B. Deguilhem, S. Grolleau, M. Gerard, F. Suard, and D. Riu, *J. Power Sources*, **241**, 680 (2013).
20. S. J. An, J. L. Li, C. Daniel, D. Mohanty, S. Nagpure, and D. L. Wood, *Carbon*, **105**, 52 (2016).
21. Q. Liu, C. Du, B. Shen, P. Zuo, X. Cheng, Y. Ma, G. Yin, and Y. Gao, *RSC Adv.*, **6**, 88683 (2016).
22. M. Broussely, *Advances in Lithium-Ion Batteries*, ed. W. A. van Schalkwijk (Springer, Boston, MA) p. 393 (2007).
23. M. Petzl, M. Kasper, and M. A. Danzer, *J. Power Sources*, **275**, 799 (2015).
24. J. Cannarella and C. B. Arnold, *J. Electrochem. Soc.*, **162**, A1365 (2015).
25. R. D. Minter, D. Juarez-Robles, C. Fear, Y. Barsukov, and P. P. Mukherjee, *JOVE*, **e57735**, 135 (2018).
26. R. Guo, L. G. Lu, M. G. Ouyang, and X. N. Feng, *Sci. Rep.*, **6**, 30248 (2016).
27. D. Juarez-Robles, A. A. Vyas, C. Fear, J. A. Jeevarajan, and P. P. Mukherjee, *J. Electrochem. Soc.*, **167**, 1 (2020).
28. A. Mistry, H. R. Palle, and P. P. Mukherjee, *Appl. Phys. Lett.*, **114**, 023901 (2019).
29. A. N. Mistry, K. Smith, and P. P. Mukherjee, *Acs Appl Mater Inter*, **10**, 28644 (2018).
30. X.-G. Yang, Y. Leng, G. Zhang, S. Ge, and C.-Y. Wang, *J. Power Sources*, **360**, 28 (2017).
31. J. Neubauer and A. Pesaran, *J. Power Sources*, **196**, 10351 (2011).
32. M. Uitz, M. Sternad, S. Breuer, C. Täubert, T. Traußnig, V. Hennige, I. Hanzu, and M. Wilkening, *J. Electrochem. Soc.*, **164**, A3503 (2017).
33. A. Mandli, A. Kaushik, R. Patil, A. Naha, K. Hariharan, S. M. Kolake, S. Han, and W. Choi, *Int. J. Energ. Res.*, **43**, 1 (2019).
34. D. Juarez-Robles, C. F. Chen, Y. Barsoukov, and P. P. Mukherjee, *J. Electrochem. Soc.*, **164**, A837 (2017).
35. I. Bloom, L. K. Walker, J. K. Basco, D. P. Abraham, J. P. Christophersen, and C. D. Ho, *J. Power Sources*, **195**, 877 (2010).
36. H. M. Dahn, A. J. Smith, J. C. Burns, D. A. Stevens, and J. R. Dahn, *J. Electrochem. Soc.*, **159**, A1405 (2012).
37. I. Bloom, A. N. Jansen, D. P. Abraham, J. Knuth, S. A. Jones, V. S. Battaglia, and G. L. Henriksen, *J. Power Sources*, **139**, 295 (2005).
38. L. Mu et al., *Nano Lett.*, **18**, 3241 (2018).
39. H. F. Li, J. K. Gao, and S. L. Zhang, *Chinese J Chem*, **26**, 1585 (2008).
40. L. Zhang, Y. Ma, X. Cheng, C. Du, T. Guan, Y. Cui, S. Sun, P. Zuo, Y. Gao, and G. Yin, *J. Power Sources*, **293**, 1006 (2015).
41. A. Mistry, C. Fear, R. Carter, C. Love, and P. P. Mukherjee, *ACS Energy Lett.*, **4**, 156 (2018).
42. F.-M. Wang, M.-H. Yu, Y.-J. Hsiao, Y. Tsai, B. J. Hwang, Y.-Y. Wang, and C.-C. Wan, *Int. J. Electrochem. Sc.*, **6**, 1014 (2011).
43. P. Barai, B. Huang, S. J. Dillon, and P. P. Mukherjee, *J. Electrochem. Soc.*, **163**, A3022 (2016).
44. S. Erol, M. E. Orazem, and R. P. Muller, *J. Power Sources*, **270**, 92 (2014).